Research Square

Preprints are preliminary reports that have not undergone peer review.
They should not be considered conclusive, used to inform clinical practice,
or referenced by the media as validated information.

Multifunctional BN-Enabled $Li_7La_3Zr_2O_{12}$ Composite Electrolytes with Enhanced Toughness and Ionic Conductivity

Muhammad Mujtaba Syed
Khalifa University of Science and Technology
Balamurugan Thirumalraj
Khalifa University of Science and Technology
Jing Zhang
Chinese Academy of Sciences
Abdallah Kamal
Khalifa University of Science and Technology
Dawei Zhang
Khalifa University of Science and Technology
Baosong Li
Khalifa University of Science and Technology
Qingwen Li
Chinese Academy of Sciences
Kin Liao
Khalifa University of Science and Technology
Lianxi Zheng
lianxi.zheng@ku.ac.ae

Khalifa University of Science and Technology

Research Article

Keywords: Ultrafast joule heating, Composite solid electrolyte, Multifunctional ceramics, Hexagonal boron nitride, Solid-state lithium batteries

Posted Date: September 2nd, 2026

DOI: https://doi.org/10.21203/rs.3.rs-10651590/v1

License: This work is licensed under a Creative Commons Attribution 4.0 International License.
Read Full License

Additional Declarations: No competing interests reported.

Abstract

The development of mechanically robust and ionically conductive solid electrolytes is essential to ensure fast electrochemical kinetics, dendrite suppression, enhanced safety, and stable cycling performance in solid-state lithium batteries. However, simultaneously achieving these properties remains a critical challenge. Here, we report an ultrafast sintering strategy to fabricate hexagonal boron nitride (BN)-reinforced $Li_7La_3Zr_2O_{12}$ (LLZO) composite electrolytes with well-balanced ionic conductivity and mechanical strength. The optimized LLZO/BN composite demonstrates enhanced densification, reduced grain-boundary resistance, improved ionic conductivity, and a substantial increase in toughness compared to pristine LLZO and a conventionally sintered LLZO. Only a 0.5 wt.% addition of BN resulted in a 12-fold increase in toughness from ~ 5.8 MJ/m^3 to ~ 70.2 MJ/m^3 and approximately a 2.5-fold enhancement in ionic conductivity, from 4.48×10^{-6} S/cm to 1.1×10^{-5} S/cm. This study reveals that BN not only acts as a sintering aid to promote densification but also reacts with Li_2CO_3 to form Li_3BO_3, thereby reducing interfacial resistance and facilitating Li-ion transport. This work demonstrates that fast sintering combined with BN is a scalable and efficient approach to synthesize mechanically robust and electrochemically improved garnet electrolytes for practical solid-state battery applications.

1. Introduction

Solid-state lithium-ion batteries (SSLBs) represent a significant advancement in energy storage technology, offering notable benefits over traditional liquid-electrolyte batteries, such as high energy density (per unit volume), enhanced safety (dendrite suppression, leak-free), high thermal & chemical stability, and prolonged cycling lifespan [1–3]. In SSLBs, solid electrolytes (SEs) play a multifunctional role by simultaneously serving as ionic conductors and electron separators, thereby motivating extensive research into oxide, sulfide, and polymer-based SEs [3–6]. Among various SE garnet-type electrolytes, $Li_7La_3Zr_2O_{12}$ (LLZO) has garnered significant interest, owing to its high theoretical ionic conductivity (~ 10^{-3} S/cm at room temperature), electrochemical stability against lithium metal, and wide operational voltage window (up to 6V) [7–9]. Despite these advantages, achieving a balance between electrochemical and mechanical properties in LLZO-based ceramics remains a critical challenge for the practical realization of SSLBs.

A critical limitation of LLZO garnets and most ceramic electrolytes is their intrinsic brittleness, which is often overlooked in many studies [7]. The low fracture toughness can lead to crack initiation and propagation during cell assembly or electrochemical cycling. Such mechanical degradation not only accelerates interfacial instability but also facilitates lithium dendrite penetration, ultimately causing internal short circuits and catastrophic cell failure, thereby compromising safety, lifetime, and cycling stability [10, 11]. To address these challenges, previous studies have explored the use of nanoscale reinforcements such as carbon nanotubes, graphene, and other secondary ceramics to improve the mechanical properties of ceramics [12]. Another widely adopted strategy involves developing composite electrolytes by incorporating polymers such as PEO, PEA, epoxy, and PVDF, thereby improving flexibility

and mechanical stability [13, 14]. In addition, interfacial engineering approaches have been explored, such as forming artificial solid electrolyte interphases (SEIs), for example, LiF/Cu layers at the Li_6PS_5Cl interface, to improve interfacial stability [15]. Despite this progress, significant limitations remain. The electrically conductive reinforcements can increase the risk of an internal short circuit due to the growth of lithium dendrites. On the other hand, insulating additives and polymer-rich architectures often enhance mechanical strength at the expense of ionic conductivity (IC). Thus, developing a strategy that simultaneously enhances mechanical robustness without losing electrochemical performance remains an unresolved challenge.

In addition to intrinsic brittleness, the IC of garnet electrolytes is strongly influenced by their chemical composition and microstructure developed during the synthesis. Conventional solid-state synthesis of garnets is widely accepted due to its simplicity, low cost, and scalability. However, this method typically requires an elevated sintering temperature (> 1000°C) for prolonged periods (> 10 hours). This exposure results in significant Li-ion volatilization, which, in turn, significantly reduces the ionic conductivity (IC) required for practical applications [16, 17]. High lithium loss transforms $Li_7La_3Zr_2O_{12}$ to $La_2Zr_2O_7$ phase, which increases the grain boundary resistance and blocks Li-ion transport. To address these challenges, various strategies have been developed, including doping [18], the use of sintering aids [9, 19], and advanced processing/sintering techniques such as spark plasma sintering, microwave-assisted sintering, and flash sintering [12, 17, 20, 21]. While these approaches can partially improve densification and conductivity, they often involve trade-offs, such as increased compositional complexity, limited scalability, or insufficient control over grain-boundary chemistry. Another critical challenge in garnet electrolytes is the formation of a Li_2CO_3 (LCO) passivation layer on the surface of air-exposed LLZO [22]. This layer introduces high interfacial resistance between the SE and electrodes, thereby limiting Li-ion conductivity [23, 24]. Therefore, a scalable strategy that can simultaneously suppress lithium loss, optimize the microstructure, and effectively engineer grain-boundary resistance remains highly desirable.

In this work, we address the aforementioned challenges by incorporating h-BN as a multifunctional additive into LLZO, combined with ultrafast Joule heating (UFJH) processing. BN provides several advantages; it acts as an effective sintering aid, improving the material's compressive energy absorption (toughness), serves as an electronic insulator, and more importantly, actively participates in modifying grain-boundary chemistry by reacting with LCO to form Li_3BO_3 (LBO). When combined with UFJH, which enables densification within seconds while minimizing lithium loss, this approach overcomes the key limitations associated with conventional thermal processing. It is demonstrated that only 0.5wt.% addition of BN to LLZO, combined with UFJH, not only provides better toughness but also offers reasonable ionic conductivity under ambient conditions. Overall, this study provides a facile and scalable approach towards improving the mechanical robustness and electrochemical performance of LLZO-based electrolytes for next-generation SSLBs.

2. Experimental Section

2.1 Synthesis of LLZO

The $Li_7La_3Zr_2O_{12}$ (LLZO) powder was synthesized by a common solid-state reaction. Initially, Li_2CO_3 (99.9%, Sigma-Aldrich), La_2O_3 (99.9%, Sigma-Aldrich), and ZrO_2 (99.99%, Sigma-Aldrich) were precisely weighed and combined in stoichiometric ratios. The mixture was then subjected to mechanical ball milling with 2-propanol using zirconia balls in a zirconia jar for 24 hours, followed by drying and thermal treatment in air at 950°C for 12 hours. The resulting LLZO powder was subsequently ground manually and stored in a container.

2.2 Synthesis of LLZO and LLZO/BN Composite Pellets

The LLZO and LLZO/BN composite pellets were prepared using the UFJH approach. First, 2.5 g of LLZO powder was dispersed in 25 mL of ethanol and sonicated for 1 hour. Next, varying amounts of commercially available h-BN (0.5 wt.%, 1 wt.%, 2.5 wt.%, 5%, and 10 wt.%) were added to the LLZO mixture and thoroughly blended in a planetary mill with zirconia balls for 24 hours. The resulting LLZO/BN composite was then filtered, washed with ethanol, and dried for 24 hours in a hot air oven at 60°C. After drying, the LLZO/BN composite was pelletized using a hydraulic press at 3 tons in a 10 mm pellet die. Finally, the LLZO/BN pellets were sintered at ~ 950°C using UFJH, as illustrated in Figure S1. UFJH was achieved by passing direct current through activated graphite felt (99.9%) purchased from a fuel cell store. A graphite felt measuring 15 cm by 2 cm and approximately 2 mm thick was used to sinter the pellets. The pellets were sandwiched in a pocket of graphite felt, and heat was produced by resistive heating (I^2RT) [17], where I is current, R is resistance, and t is time. In UFJH, the quick thermal shock (through radiation and conduction of heat) speeds up particle fusion, reducing LLZO ceramic sintering time and temperature while maintaining Li concentration [17]. The temperature inside the pocket was measured using Fluke's infrared (IR) thermal imaging camera. A DC power supply was used to reach approximately 950°C within a few seconds under ambient conditions. Figure S1a illustrates the temperature profile employed for ultrafast sintering of pellets. Each pellet was sintered for approximately 30 seconds at fast heating and cooling rates. The schematic of the Joule-heating setup is shown in Figure S1b. Figure S1c shows temperature as a function of current (in Amperes). A temperature of approximately 966°C was reached at 10.5 amperes in ~ 30 seconds. Figure S1d displays images from the IR camera, showing a rapid increase in temperature from room temperature (~ 26°C) to a peak of ~ 966°C.

2.3 Materials Characterization

The material's crystal structure was examined via X-ray diffraction (XRD). XRD was conducted using Cu Kα radiation at 30 kV and 10 mA, with a scan rate of 0.05 degrees per second over a 2 theta range of 10° to 60°, employing a Bruker D2 Phaser. The flat surface, cross-sectional morphology, and Energy Dispersive Spectroscopy (EDS) analysis of the pellets were examined using a field-emission scanning electron microscope (JEOL JSM-7610F FE-SEM). Fourier transform infrared (FTIR) spectra were recorded in the range of 550 to 4000 cm^{-1} utilizing a Fourier transform infrared spectrometer and imaging system (Spotlight 400, PerkinElmer Instrument, Inc.). The X-ray photoelectron spectroscopy

(XPS) spectra of the electrolyte pellets were obtained using the Escalab Xi + X-ray Photoelectron Spectrometer. Thermogravimetric analysis (TGA) of electrolytes in a nitrogen atmosphere was performed using a Simultaneous Thermal Analyzer-STA 449 F5 Jupiter apparatus. An Instron 5948 universal testing machine was used for compression testing at a strain rate of 0.05 mm/min.

2.4 Ionic Conductivity Measurement

The ionic conductivity of the as-prepared LLZO garnet SE and the LLZO/BN composite SE was examined using electrochemical impedance spectroscopy (EIS). To achieve good electrical contact and reduce interfacial resistance, pellets were ground, polished, and coated with a silver paste. The pellets were subsequently positioned between two polished stainless-steel plates, within a custom-designed Swagelok-type cell. The EIS measurements were performed using a Potentiostat at room temperature over a frequency range of 0.1 MHz to 100 mHz and an oscillation amplitude of 10 mV. Measurements were conducted under ambient conditions, unless otherwise stated.

3. Results and Discussion

3.1 Synthesis and Characterization of LLZO/BN Composite

Figure 1 schematically presents the step-by-step synthesis procedure for preparing LLZO/BN composite electrolytes using UFJH. First, the as-prepared LLZO powder is mixed with a controlled amount of BN using a planetary ball mill with Zirconia balls. The resulting mixed powder is then uniaxially pressed with a 10 mm die using a hydraulic press to prepare green pellets. The green pellets are subsequently subjected to UFJH, in which they are sandwiched between graphite felts. UFJH enables simultaneous sintering and densification of the LLZO/BN composite while minimizing lithium volatilization. During this process, BN not only acts as a physical reinforcement but also contributes to grain-boundary modification, promoting the *in-situ* formation of Li_3BO_3 as a sintering aid. As illustrated in the final stage of Fig. 1, the resulting pellets are dense ceramic composites suitable for mechanical and electrochemical characterization.

The purity and crystalline nature of the LLZO/BN composite were analyzed by XRD crystallography, as shown in Fig. 2a. The pristine LLZO retains its pure tetragonal phase, matching the PDF card number 98-024-6816. In addition, all the corresponding LLZO peaks are retained after the addition of 0.5 wt.% until 10 wt.% BN. This indicates that the addition of BN and UFJH does not induce any detectable phase transformation or decomposition of the LLZO. The weak reflections associated with BN are more visible at higher BN loadings, highlighting the presence of BN as a secondary phase without disrupting the garnet lattice.

ATR-FTIR spectra of pristine LLZO, pure BN, and LLZO/BN composites (Figs. 2b and Figure S2a) are analyzed to confirm the surface chemistry of the composite material. FTIR of BN shows expected out-of-plane vibration at ~ 760 cm^{-1} and in-plane vibration broadband at ~ 1350 cm^{-1}. It is well established that LLZO forms LiOH and Li_2CO_3 at the surface upon exposure to air [23]. For neat LLZO as well as

LLZO/BN composites, Li_2CO_3-related peaks are visible at ~ 860 cm^{-1} and ~ 1415 cm^{-1}. The peak at ~ 814 cm^{-1}, which is absent in pristine LLZO and does not coincide with the BN peak, is attributed to LBO vibrations in the ~ 700–1000 cm^{-1} region, which are characteristic of borate B-O stretching[25] with a possible overlap from the BN out-of-plane mode and carbonate contributions. These results imply that BN facilitates the formation of LBO at the composite surface.

The thermal stability of pristine LLZO and LLZO/BN composites was further evaluated using thermogravimetric analysis (TGA), as shown in Fig. 2c. TGA data indicate negligible weight loss up to 190°C for pristine LLZO, followed by a gradual weight loss of around 2.0% between 190°C and 500°C. This loss is attributed to the removal and/or decomposition of Li_2CO_3/LiOH normally present at the surface of LLZO [26]. With 0.5 wt.% BN addition in LLZO, no noticeable weight loss was observed until 280°C, followed by a weight loss of 1.2 % util 500°C. Similarly, increasing the BN to 1 wt.% and 2.5 wt.% further delayed the initial mass loss and the amount of weight loss. The composite with 5 wt.% BN shows noticeable weight loss only after 370°C, and the total loss remained less than 1% up to 500°C. The addition of BN to LLZO forms relatively stable compounds such as Li_3BO_3 and Li_3BN_2, thereby improving thermal stability and reducing weight loss [27]. The thermal energy provides sufficient thermodynamic driving force responsible for the formation of Li_3BO_3, the related governing chemical equation can be written as [28],

$$2BN + 3Li_2CO_3 + \frac{3}{2}O_2 \xrightarrow{\mathrm{UFJH},\ \mathrm{Air}} 2Li_3BO_3 + 3CO_2(\uparrow) + N_2(\uparrow)$$

Above 600°C, weight loss can be attributed to lithium volatility or the evaporation of other trace compounds, such as Li_2CO_3. At temperatures above 700°C, the loss is primarily due to Li evaporation and exhibits a linear decrease in weight [9]. The total weight loss is highest in pristine LLZO (around 3.7%), whereas the presence of BN significantly suppresses weight loss at higher temperatures. The thermal stability increases as the wt.% of BN increases; maximum weight losses of approximately 2.3%, 2.0%, 1.7%, and 1.5% were observed for 0.5 wt.%, 1 wt.%, 2.5 wt.%, and 5 wt.%, respectively. Lastly, for 10 wt.% BN addition, a negligible weight loss of only 0.2% was observed across the entire temperature range. These results indicate that LLZO/BN composites exhibit superior thermal stability in contrast with pristine LLZO.

FTIR and TGA analyses indicated that the addition of BN in LLZO/BN composites promotes the formation of LBO, while suppressing the non-conducting Li_2CO_3. To further probe the surface chemistry, X-ray photoelectron spectroscopy (XPS) was performed on pristine LLZO and LLZO/BN composite. The survey spectra confirm the presence of constituent elements in LLZO and LLZO/BN, as shown in the supplementary Figures S2b and S2c, respectively. The detectable atomic percentages of Boron and Nitrogen in the composite further confirm the successful incorporation of BN, as given in Supplementary Table S1. High-resolution XPS spectra of Li 1s, oxygen O 1s, and C 1s were deconvoluted (Figs. 2d to 2i) to compare the contributions of LLZO, LBO, and LCO species [28, 29]. The LLZO/BN composite exhibits additional peaks at approximately 56.8 eV and 530.7 eV in the Li 1s and O 1s spectra; these peaks can be associated with Li-O and borate-type (BO_3^{3-}) species in LBO. Furthermore, the deconvoluted B 1s

spectrum shows an additional BO_3^{3-} peak at around 192 eV, as presented in Figure S2d. Additionally, the fitted fraction of carbonate (CO_3^{2-}) in the O 1s spectrum decreases from 66.5% for pristine LLZO to 37.3% for LLZO/BN, while the carbonate percentage in the C 1s spectrum decreases from 50.0% to 23.1%. Carbonate species related to LCO are typically found at ~531.5–532 eV in O 1s, and ~289.5–290 eV in C 1s [7], and the decrease in the carbonate fraction provides strong evidence of LCO suppression on the LLZO/BN surface. Therefore, the XPS results support the FTIR/TGA observations and indicate that BN addition facilitates the consumption of surface LCO into an LBO-rich surface/grain-boundary phase in the LLZO/BN composite.

3.2 Surface/ Cross-Sectional Morphology and Elemental Composition of LLZO/BN Composite

The surface and cross-sectional morphology of pristine LLZO and LLZO/BN composites were examined by Field Emission Scanning Electron Microscopy (FESEM), as shown in Figs. 3a-3r. The SEM images of pristine LLZO reveal a smooth but relatively low density, as reflected in the measured density values (Table S2). This observation can be attributed to the higher intergranular spaces among the garnet crystals, as shown in Figs. 3a to 3c. At low sintering temperature, poor densification is commonly observed in garnets without sintering aids due to limited mass transport [9, 30]. In contrast, the addition of BN (up to 5 wt.%) results in a relatively uniform, denser, and well-aggregated microstructure, as depicted in Figs. 3d to 3o. This densification can be attributed to BN's role as a sintering aid, which facilitates mass transport and promotes densification during UFJH. However, when further increasing the BN content to 10 wt.%, the microstructure becomes non-uniform, as shown in Figs. 3p- 3r. The excess BN content in the composite leads to BN aggregation, which traps the volatile species (CO_2 and H_2O). This gas stagnation leads to irregular pellet expansion and poor densification during sintering, as evidenced through SEM, Fig. 3r.

These microstructural observations are in good agreement with the measured pellet densities (Table S2). Notably, only 0.5 wt.% addition of BN results in the highest relative density of ~ 93.6%, followed by a composite with 1 wt. % BN with a comparable value of ~ 92.3%. Increasing BN content further decreases density, reaching ~ 86.9% at 2.5 wt.% BN, ~ 85.1% for 5 wt.% BN and a minimum of 73.4% for 10 wt.% BN. Again, this decrease in densification can be attributed to BN aggregation at higher concentrations, which leads to the formation of voids. As a result, the LLZO + 0.5 wt.% BN composite exhibits a more uniform structural arrangement, high density, and the lowest grain-boundary porosity. Thus, LLZO/0.5 wt.% BN is identified as the optimal composite for further investigations of its mechanical and electrochemical properties.

The elemental composition and mapping of the as-prepared LLZO/BN composite were further characterized by energy-dispersive X-ray spectroscopy (EDS), as illustrated in Fig. 4. The EDS analysis of the LLZO/BN composite shows the corresponding elements, such as B, N, La, Zr, and O, as the principal constituents in the EDS spectrum (Fig. 4a). The corresponding quantitative atomic weight percentage of

each element is shown in Fig. 4b. The surface morphology of the LLZO/BN composite observed by SEM (Fig. 4c) appears compact and homogeneous, in agreement with the densification trends discussed earlier. Furthermore, the elemental mapping images of the LLZO/BN composite in Figs. 3d-3h provide insight into the spatial distribution of individual elements. Boron (Fig. 4d) and nitrogen (Fig. 4e) appear to be uniformly distributed across the scanned region, indicating that BN is well dispersed throughout the LLZO matrix. Similarly, La (Fig. 4f), Zr (Fig. 4g), and O (Fig. 4h) exhibit a homogeneous distribution, confirming the structural continuity of the garnet LLZO phase within the composite.

3.3 Mechanical Properties of LLZO/BN Composite

For practical applications such as solid-state batteries, an electrolyte should attain sufficient toughness to sustain compressive loads and suppress dendrite formation during battery cycling [31]. For cyclic stability in solid-state batteries, a stack pressure of several hundred MPa is recommended during both fabrication and operation to prevent the penetration of Li dendrites [32, 33]. In this study, we measured the mechanical performance of SEs during compression, as depicted in Fig. 5a. Identical samples of LLZO and LLZO/BN composite (at least three samples each) with a diameter of 10 mm and a thickness of ~ 0.9 mm ± 0.1 were compressed uniaxially between two parallel plates at a strain rate of 0.05 mm/min^{-1}. The selected acquired stress-strain profiles for pristine LLZO, LLZO + 0.5 wt.% BN, LLZO + 1 wt.% BN, LLZO + 2.5 wt.% BN, LLZO + 5 wt.% BN, and LLZO + 10wt.% BN are shown in Figs. 5b and 5c. In general, the initial region shows strain corresponding to the progressive contact between the sample and the compression plates. After that, an almost linear relationship between stress and strain is observed, reflecting elastic behavior. In the final phase, stress-strain curves form a plateau or a sudden drop, indicating densification and/or material failure [34, 35].

The incorporation of BN fillers as a reinforcing material significantly improves the mechanical performance of LLZO/BN composites. The dense microstructure and minimal porosity in the composites can be correlated with the enhanced mechanical properties during the compression test. Table S3 presents the comparison of toughness and strain values at 150 MPa for pristine LLZO and LLZO/BN composites. Pristine LLZO exhibits a toughness of only ~ 5.8 $MJ.m^{-3}$ and begins to densify at a compressive stress of 50 MPa. In contrast, only a 0.5 wt.% addition of BN resulted in the highest toughness of ~ 70 MJ/m^3 and the lowest compressive strain of ~ 0.082 at 150 MPa (Fig. 5d). This excellent performance can be attributed to a highly dense microstructure, crack deflection, and a bridging mechanism introduced by the addition of BN, as illustrated in Fig. 5e and previously observed in [12, 36]. As the BN content is increased to 5 wt.%, a sharp decrease in toughness is observed, whereas strain increases linearly (at a fixed stress of 150 MPa). Further increasing the BN content to 10 wt.% resulted in a minimum toughness of 2.2 MJ/m^3 and failure at the beginning of the test. LLZO + 10 wt.% BN sample displayed an irregular stress-strain behavior throughout the test, as shown in the magnified view of stress-strain curves in Fig. 5c. This can primarily be attributed to higher BN content, which leads to BN aggregation; during sintering, it expands, creating pores, as observed previously in Fig. 3r.

3.4 Ionic Conductivity of LLZO/BN Composite

The resulting Nyquist plots of the EIS spectra for the pristine LLZO and LLZO/BN composites are presented in Fig. 6a, and their zoomed-in view is presented in Fig. 6b. The suppressed semicircle in the high-frequency region of the Nyquist plot is associated with the impedance of the grain and the grain boundary, and the line in the low-frequency region is associated with the interfacial resistance between the electrolyte and steel blocking electrodes. Figure S3 shows the equivalent circuit used to mimic the behavior of pristine LLZO and LLZO/BN composites. The Nyquist plot of pristine LLZO clearly shows a semicircle in the high-frequency region, followed by a curve and a tail, as shown in Figure S3a [7, 37]. In contrast, when 0.5 wt.% BN was added, the semicircle is suppressed in the high-frequency region, followed by a tail, indicating a significant decrease in grain boundary resistance. This behavior can be simply mimicked using the equivalent circuit presented in Figure S3b. As the BN content increased to 1 wt.%, the semicircle reappeared, and as the content was further increased to 2.5 wt.%, the semicircle radius increased, indicating a sharp increase in grain boundary resistance. Further increasing the BN to 5 wt.% or higher led to an exponential increase in resistance, and we were unable to obtain usable data.

The point on the real axis where a semicircle and the tail intersect gives the total resistance of the electrolyte and is used to calculate the ionic conductivity [38]. Figure 6c and Table S4 present ionic conductivity calculated using the total resistance of LLZO and LLZO/BN composites. Pristine LLZO achieved an IC of 4.45×10^{-6} S/cm. In contrast, the composite with 0.5 wt.% BN achieved the highest ionic conductivity of ~ 11×10^{-6} S/cm and the lowest resistance. This enhancement in ionic conductivity is closely correlated with the densification behavior of the composites. The LLZO + 0.5 wt.% BN sample, which exhibits the highest relative density (~ 93.6%), also delivers the lowest grain-boundary resistance and the highest ionic conductivity among all compositions. As the BN content increases further, the IC decreases, and total resistance increases. Figure 6d presents the schematic of the Li ion conduction in the LLZO/BN composite, where Li_3BO_3 helps fill the grain boundary and allows Li ions to pass, thus improving the IC. For the sake of wider applicability of this approach, a different composite using Al-doped LLZO (LALZO) with 0.5 wt.% BN is also prepared using UFJH under the same conditions. LALZO/BN achieved an IC of 97.4×10^{-6} S/cm, which is about 8.8 times higher than LLZO/BN, as shown in Figure S4. This increment is due to the well-established fact that Al in LALZO helps achieve a more ionic-conducting phase in contrast with LLZO [39]. The Arrhenius plot in Fig. 6e is used to analyze the temperature dependence of ionic conductivity. The IC increases with temperature, with an activation energy of 0.34 eV, which is lower than the value reported in the literature [9, 40]. This implies that Li-ion movement is facilitated by a well-aggregated structure of the LLZO/BN composite.

3.5 Comparison of LLZO/BN Composites Prepared using UFJH and Conventional Sintering

The mechanical and electrochemical properties of LLZO + 0.5 wt.% BN pellets prepared using UFJH were compared with those fabricated using conventional sintering (CS), as shown in Fig. 7 and summarized in Table S5 along with the relevant literature. The Nyquist plots in Fig. 7a clearly show a distinct electrochemical behavior for pellets sintered using UFJH and CS. The pellet prepared using CS exhibits an incomplete semicircle in the high-frequency region followed by another depressed semicircle,

indicating high grain-boundary resistance. In contrast, an UFJH-processed pellet displays a single depressed semicircle, indicating a significant reduction in grain-boundary resistance and improved IC. Additionally, the mechanical performance was also analyzed using compression stress-strain measurements of the pellets, as shown in Fig. 7b. The pellets prepared using UFJH clearly achieved enhanced mechanical properties, exhibiting higher compressive stress and lower failure strain than conventionally prepared LLZO/BN pellets.

To quantitatively compare various mechanical and electrochemical parameters, bar charts of composite pellets prepared using CS and UFJH are presented in Fig. 7c. Six key parameters are analyzed, including toughness, failure strength σ(failure), ionic conductivity (IC), relative density (RD), total resistance (Rt), and activation energy (Ea). The UFJH-processed sample consistently outperforms the conventionally sintered pellets. In contrast, pellets sintered using UFJH show a ~ 53.5% increase in toughness and a ~ 33% increase in fracture or failure strength, indicating enhanced resistance to deformation and failure. Similarly, a 3.5-fold increase in IC and a ~ 7% increase in RD are observed, indicating improved densification and efficient Li-ion transport. Furthermore, the total electrochemical resistance is reduced by a factor of ~ 3.5 compared to CS, with a ~ 16% reduction in the activation energy. These results demonstrate the notable advantages of UFJH in terms of mechanical and electrochemical performance of LLZO/BN composite electrolytes. The proposed UFJH-assisted LLZO/BN composite can be produced within seconds while simultaneously improving ionic conductivity and toughness, making it an attractive route for scalable solid-state electrolyte manufacturing.

4. Conclusions

In summary, this work presents an effective strategy for synthesizing an LLZO/BN composite electrolyte by integrating UFJH with multifunctional BN fillers. In contrast with pristine LLZO, only 0.5 wt.% addition of BN exhibits an impressive 12× increment in toughness that can be attributed to the crack deflection and bridging mechanism. Additionally, BN acts as a sintering aid, promoting densification and increasing the relative density from 78.9% to 93.6% (~ 15%), thereby producing a uniform and dense microstructure. Furthermore, BN regulates grain-boundary chemistry through the in situ formation of Li_3BO_3, which suppresses the insulating Li_2CO_3 by ~ 27% and reduces total resistance by ~ 53%. This LBO-rich interphase further creates favorable pathways for Li^+ transport, thereby lowering grain-boundary resistance and enhancing IC by 150%. BN also improves the thermal stability of LLZO and reduces weight loss by ~ 1.5 wt.%, indicating improved lithium retention during processing. These combined effects, such as enhanced densification, toughening, interfacial modification, and thermal stabilization, highlight the unique role of BN as an active filler. Moreover, the ultrafast-sintered LLZO/BN composites outperform conventionally sintered composites in terms of their mechanical and electrochemical performance. This work highlights the critical role of BN as an effective multifunctional additive in addressing key challenges in advancing SSLBs, including brittleness, Li volatility, and high interfacial resistance.

Declarations

Declaration of Interest

We have no conflicts of interest to declare.

Funding

The research work was funded by the Research and Innovation Center for Graphene and 2D Materials (RIC2D) at Khalifa University, UAE.

Author Contribution

M.M.S. conceived the study, designed the experiments, synthesized the materials, performed electrochemical and mechanical characterization, analyzed the data, prepared the figures, and wrote the original manuscript draft.B.T. contributed to the study conception and experimental design, assisted with data interpretation, and critically revised the manuscript.J.Z. provided scientific guidance, data validation, and manuscript revision.A.K.contributed to mechanical testing, analysis of mechanical properties. D.Z. assisted with data validation, and manuscript revision.B.L. assited in data collection, data validation, and manuscript revision.Q.L. contributed to scientific discussions, data interpretation, and manuscript revision.K.L. conceived and supervised the project, secured funding.L.Z. conceived and supervised the project, secured funding, guided data interpretation, and critically revised the manuscript.M.M.S. and B.T. contributed equally to this work. All authors reviewed, discussed, and approved the final manuscript.

Acknowledgements

We would like to express our gratitude to the Research & Innovation Center for Graphene and 2D Materials (RIC-2D, DP4-8434000508) and the Research & Innovation Center on CO_2 and Hydrogen (RICH) for financial and facility support. The authors acknowledge the use of AI-assisted tools to improve the visual clarity of schematic illustrations and to refine the language and structure of the manuscript.

References

1. Famprikis T et al (2019) Fundamentals of inorganic solid-state electrolytes for batteries. Nat Mater. https://doi.org/10.1038/s41563-019-0431-3
2. Kundu S et al (2022) Recent development in the field of ceramics solid-state electrolytes: I—oxide ceramic solid-state electrolytes. J Solid State Electrochem. https://doi.org/10.1007/s10008-022-05206-x

3. Manthiram A et al (2017) Lithium battery chemistries enabled by solid-state electrolytes. Nat Reviews Mater. https://doi.org/10.1038/natrevmats.2016.103
4. Fergus JW (2010) Ceramic and polymeric solid electrolytes for lithium-ion batteries. J Power Sources. https://doi.org/https://doi.org/10.1016/j.jpowsour.2010.01.076
5. Yang H, Wu N (2022) Ionic conductivity and ion transport mechanisms of solid-state lithium-ion battery electrolytes: A review. Energy Sci Eng. https://doi.org/https://doi.org/10.1002/ese3.1163
6. Quartarone E, Mustarelli P (2011) Electrolytes for solid-state lithium rechargeable batteries: recent advances and perspectives. Chem Soc Rev. https://doi.org/10.1039/c0cs00081g
7. Zhang Z et al (2019) Boron Nitride Enhanced Garnet-Type ($Li_{6.25}Al_{0.25}La_3Zr_2O_{12}$) Ceramic Electrolyte for an All-Solid-State Lithium-Ion Battery. ACS Appl Energy Mater. https://doi.org/10.1021/acsaem.9b01431
8. Han X et al (2017) Negating interfacial impedance in garnet-based solid-state Li metal batteries. Nat Mater. https://doi.org/10.1038/nmat4821
9. Zhou H et al (2024) Li_5AlO_4 -Assisted Low-Temperature Sintering of Dense $Li_7La_3Zr_2O_{12}$ Solid Electrolyte with High Critical Current Density. ACS Appl Mater Interfaces. https://doi.org/10.1021/acsami.3c17606
10. Lutkenhaus JL, Flouda P (2020) Ceramic Electrolytes Get Tough on Lithium Metal Batteries. *Matter*. https://doi.org/10.1016/j.matt.2020.06.009
11. Cheng Q et al (2019) Stabilizing Solid Electrolyte-Anode Interface in Li-Metal Batteries by Boron Nitride-Based Nanocomposite Coating. *Joule*. https://doi.org/10.1016/j.joule.2019.03.022
12. Athanasiou CE et al (2020) High-Toughness Inorganic Solid Electrolytes via the Use of Reduced Graphene Oxide. *Matter*. https://doi.org/10.1016/j.matt.2020.05.003
13. Li A et al (2020) Nacre-Inspired Composite Electrolytes for Load-Bearing Solid-State Lithium-Metal Batteries. Adv Mater. https://doi.org/10.1002/adma.201905517
14. Wang Y et al (2026) Biomimetic spatially graded electrolytes: facilitating rapid ion conduction and dendrite-mitigated operation in solid-state lithium batteries. J Colloid Interface Sci. https://doi.org/10.1016/j.jcis.2026.139989
15. Gao Q et al (2023) Dendrite-free lithium-metal all-solid-state batteries by solid-phase passivation. Nano Energy. https://doi.org/10.1016/j.nanoen.2023.108922
16. Chen S et al (2022) Ultrafast Sintering for Ceramic-Based All-Solid-State Lithium-Metal Batteries. Adv Mater. https://doi.org/10.1002/adma.202200430
17. Wang C et al (2020) A general method to synthesize and sinter bulk ceramics in seconds. Science. https://doi.org/10.1126/science.aaz7681
18. Liu D et al (2024) Enhancing ionic conductivity of garnet-type Nb-doped Li7La3Zr2O12 by cerium doping. J Rare Earths. https://doi.org/10.1016/j.jre.2023.07.012
19. Li C et al (2020) Solid-state reactive sintering of dense and highly conductive Ta-doped Li7La3Z2O12 using CuO as a sintering aid. J Mater Sci. https://doi.org/10.1007/s10853-020-05221-

1

20. Avila V et al (2021) Phase evolution during reactive flash sintering of Li6.25Al0.25La3Zr2O12 starting from a chemically prepared powder. J Eur Ceram Soc. https://doi.org/10.1016/j.jeurceramsoc.2021.02.054
21. Yang JX et al (2021) Rapid Fabrication of High-Entropy Ceramic Nanomaterials for Catalytic Reactions. ACS Nano. https://doi.org/10.1021/acsnano.1c04259
22. Shi N et al (2025) Li2CO3 contamination in garnet solid electrolyte: Origins, impacts, and mitigation strategies. Energy Storage Mater. https://doi.org/10.1016/j.ensm.2025.104173
23. Du F et al (2022) Room-temperature, all-solid-state lithium metal batteries enabled by a moderate-temperature formation method. J Mater Sci. https://doi.org/10.1007/s10853-021-06626-2
24. Kim A et al (2024) High Energy Density Ultra-thin Li Metal Solid-State Battery Enabled by a Li_2CO_3-Proof Garnet-Type Solid Electrolyte. ACS Energy Lett. https://doi.org/10.1021/acsenergylett.4c00217
25. Milewski J et al (2024) Structural Investigation of Orthoborate-Based Electrolytic Materials for Fuel Cell Applications. Energies. https://doi.org/10.3390/en17092097
26. Zhang H et al (2023) On High-Temperature Thermal Cleaning of $Li_7La_3Zr_2O_{12}$ Solid-State Electrolytes. ACS Appl Energy Mater. https://doi.org/10.1021/acsaem.3c00459
27. Li Y et al (2021) Computational study of Li3BO3 and Li3BN2 II: Stability analysis of pure phases and of model interfaces with Li anodes. Phys Rev Mater. https://doi.org/10.1103/PhysRevMaterials.5.085403
28. Zhao G et al (2024) Enhanced comprehensive performance of the LLZO series solid electrolyte via multifunctional additive. J Eur Ceram Soc. https://doi.org/10.1016/j.jeurceramsoc.2023.11.045
29. Nagao K et al (2019) Highly Stable Li/Li_3BO_3–Li_2SO_4 Interface and Application to Bulk-Type All-Solid-State Lithium Metal Batteries. ACS Appl Energy Mater. https://doi.org/10.1021/acsaem.9b00470
30. Zhao G et al (2024) Enhanced comprehensive performance of the LLZO series solid electrolyte via multifunctional additive. J Eur Ceram Soc. https://doi.org/10.1016/j.jeurceramsoc.2023.11.045
31. Xie H et al (2019) Consolidating the grain boundary of the garnet electrolyte LLZTO with Li_3BO_3 for high-performance $LiNi_{0.8}Co_{0.1}Mn_{0.1}O_2$/$LiFePO_4$ hybrid solid batteries. J Mater Chem A. https://doi.org/10.1039/C9TA03263K
32. Pan H et al (2024) A solid-state lithium-ion battery with micron-sized silicon anode operating free from external pressure. Nat Commun. https://doi.org/10.1038/s41467-024-46472-9
33. Wu Q et al (2023) Electro-Chemo-Mechanical Failure Mechanisms of Solid-State Electrolytes. Batteries Supercaps. https://doi.org/10.1002/batt.202300321
34. Ndubuaku O et al (2018) The effect of material stress-strain characteristics on the ultimate stress and critical buckling strain of flat plates subjected to uniform axial compression. Constr Build Mater. https://doi.org/10.1016/j.conbuildmat.2018.06.100

35. Mat Samudin I et al (2025) Stress strain curve analysis of sheet based TPMS structures in quasi static compression test: A review. J Mater Res Technol. https://doi.org/10.1016/j.jmrt.2025.04.168
36. Li X et al (2022) Study on the Mechanical and Toughness Behavior of Epoxy Nano-Composites with Zero-Dimensional and Two-Dimensional Nano-Fillers. Polymers. https://doi.org/10.3390/polym14173618
37. Vadhva P et al (2021) Electrochemical Impedance Spectroscopy for All-Solid-State Batteries: Theory, Methods and Future Outlook. *ChemElectroChem*. https://doi.org/10.1002/celc.202100108
38. Wang C et al (2023) A novel promotion strategy for microstructure and electrical performance of garnet electrolytes via Li4GeO4 additive. Ceram Int. https://doi.org/10.1016/j.ceramint.2023.03.113
39. Nasir M et al (2025) Liquid electrolyte-assisted stabilization of the LLZO/Li interface for stable lithium metal batteries. EES Batteries. https://doi.org/10.1039/D5EB00026B
40. Il'ina EA et al (2014) Lithium stoichiometry of solid electrolytes based on tetragonal Li7La3Zr2O12. Mater Res Bull. https://doi.org/10.1016/j.materresbull.2014.01.041

Figures

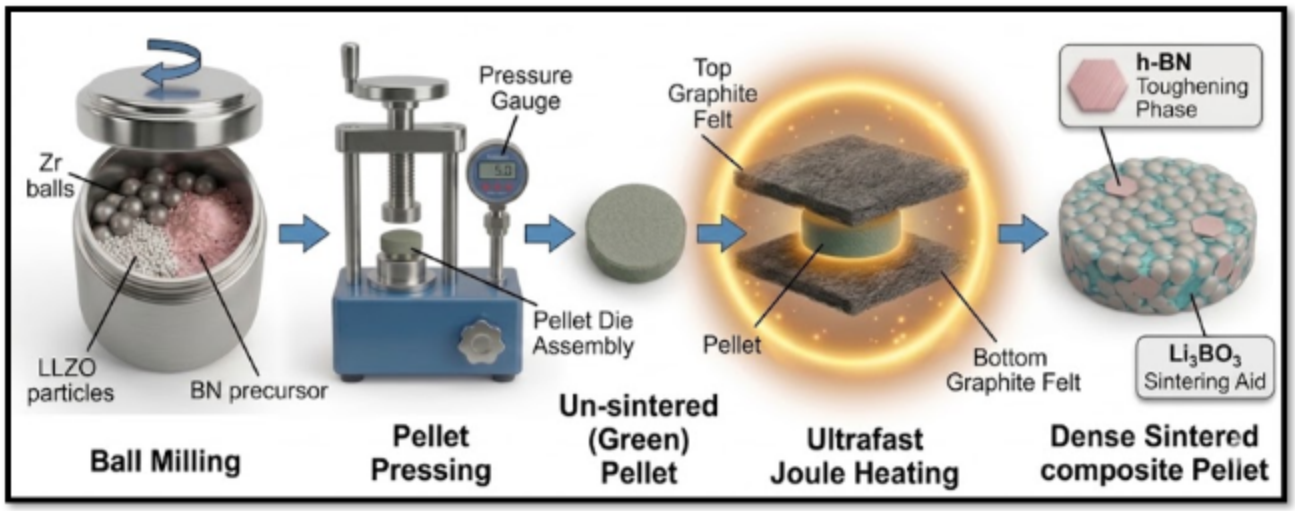

Figure 1

Schematic illustration of the fabrication process for LLZO/BN composite pellets using UFJH.

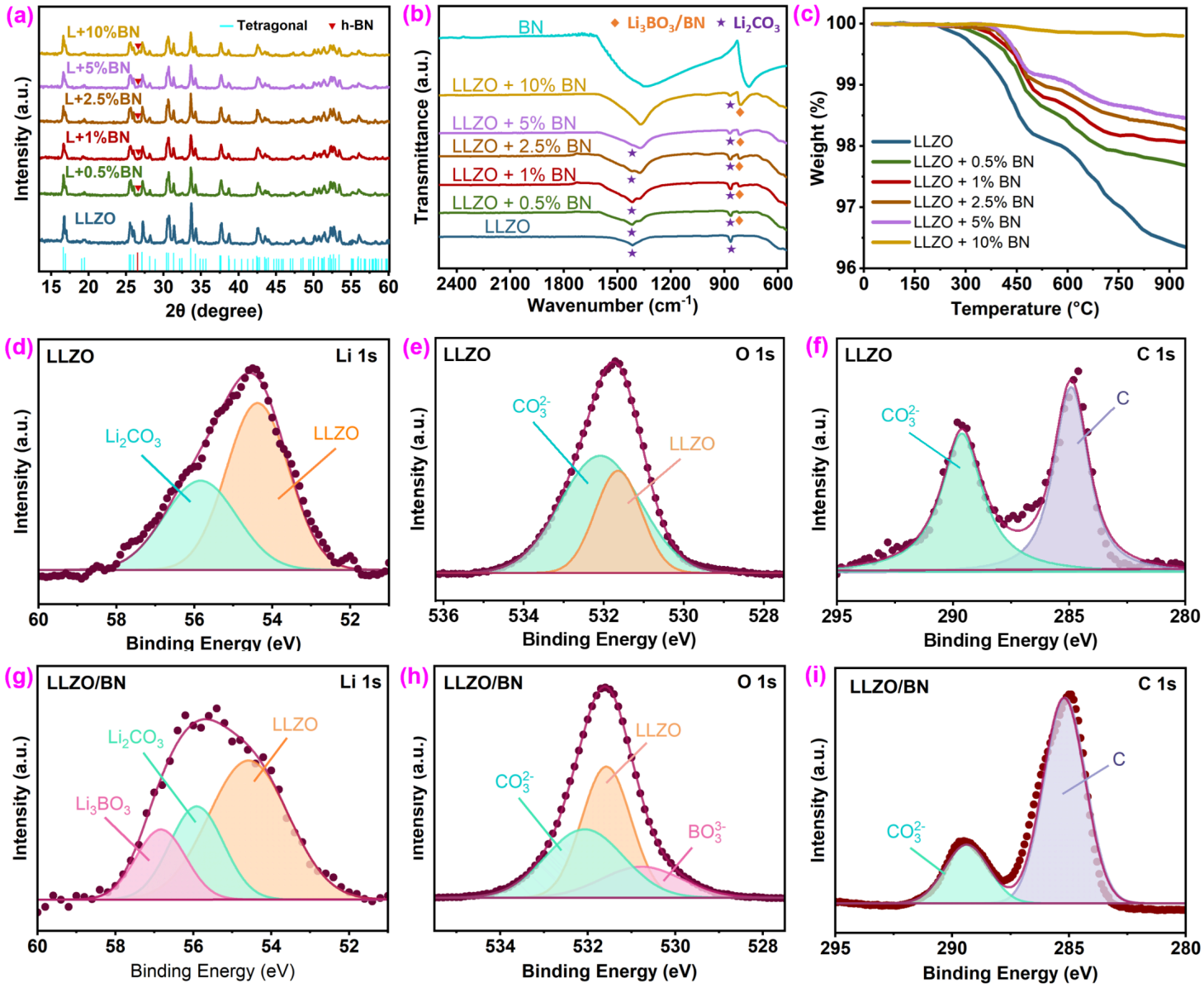

Figure 2

(a) XRD pattern of pristine LLZO and LLZO/BN composites with varying BN content. (b) FTIR spectra of pristine LLZO, BN, and LLZO/BN composites with varying BN weight percentage. (c) TGA curves of LLZO and LLZO/BN composites. High-resolution XPS spectra of pristine LLZO: (d) Li 1s, (e) O 1s, and (f) C 1s. High-resolution XPS spectra of LLZO/BN composite: (g) Li 1s, (h) O 1s, and (i) C 1s.

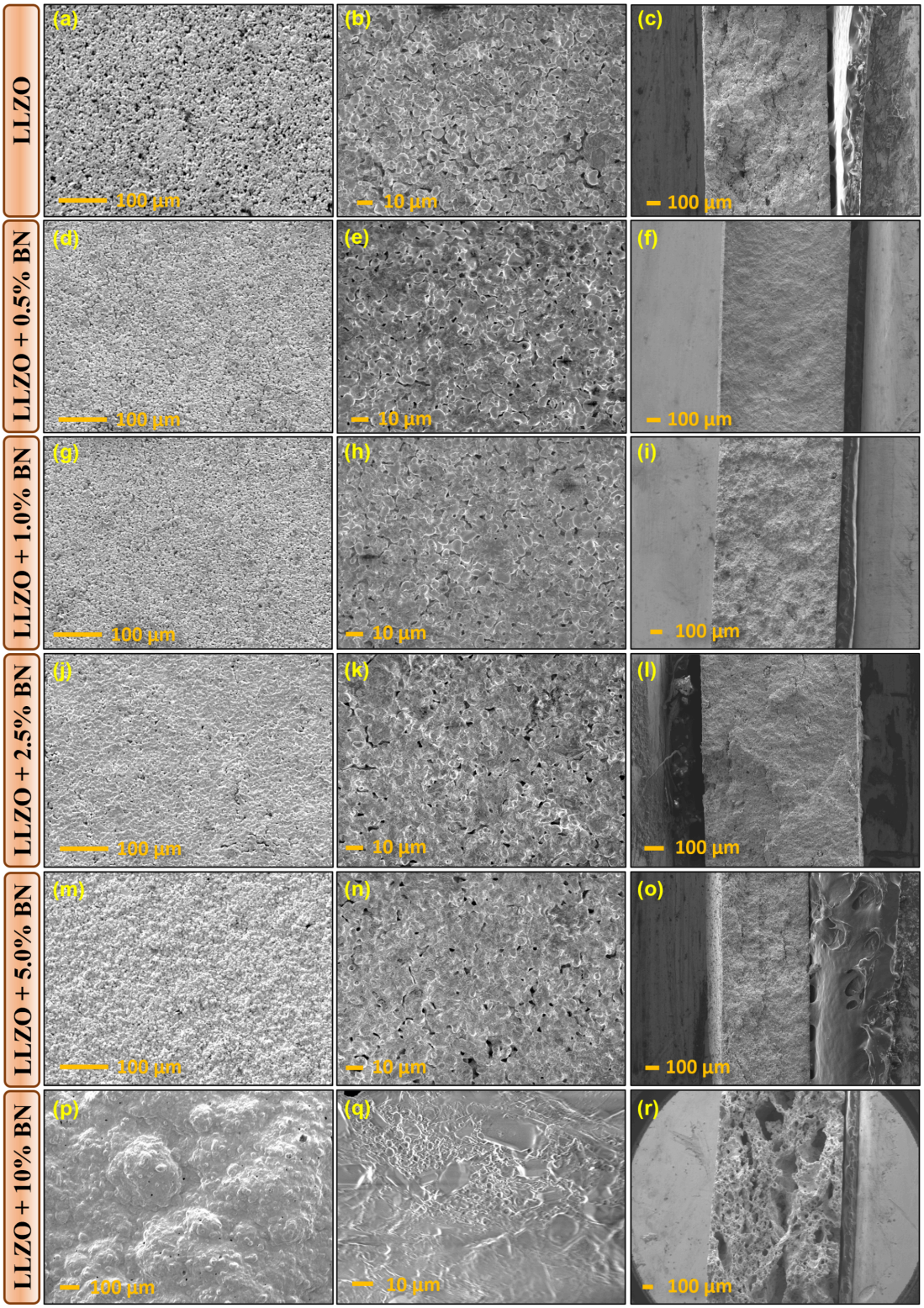

Figure 3

SEM morphology of LLZO (a, b) Surface and (c) Cross-section. SEM morphology of LLZO + 0.5 wt.% BN (d, e) Surface and (f) Cross-section. SEM morphology of LLZO + 1% BN (g, h) Surface and (i) Cross-section. SEM morphology of LLZO + 2.5% BN (j, k) Surface and (l) Cross-section. SEM morphology of LLZO + 5% BN (m, n) Surface and (o) Cross-section. SEM morphology of LLZO + 10% BN (p, q) Surface and (r) Cross-section.

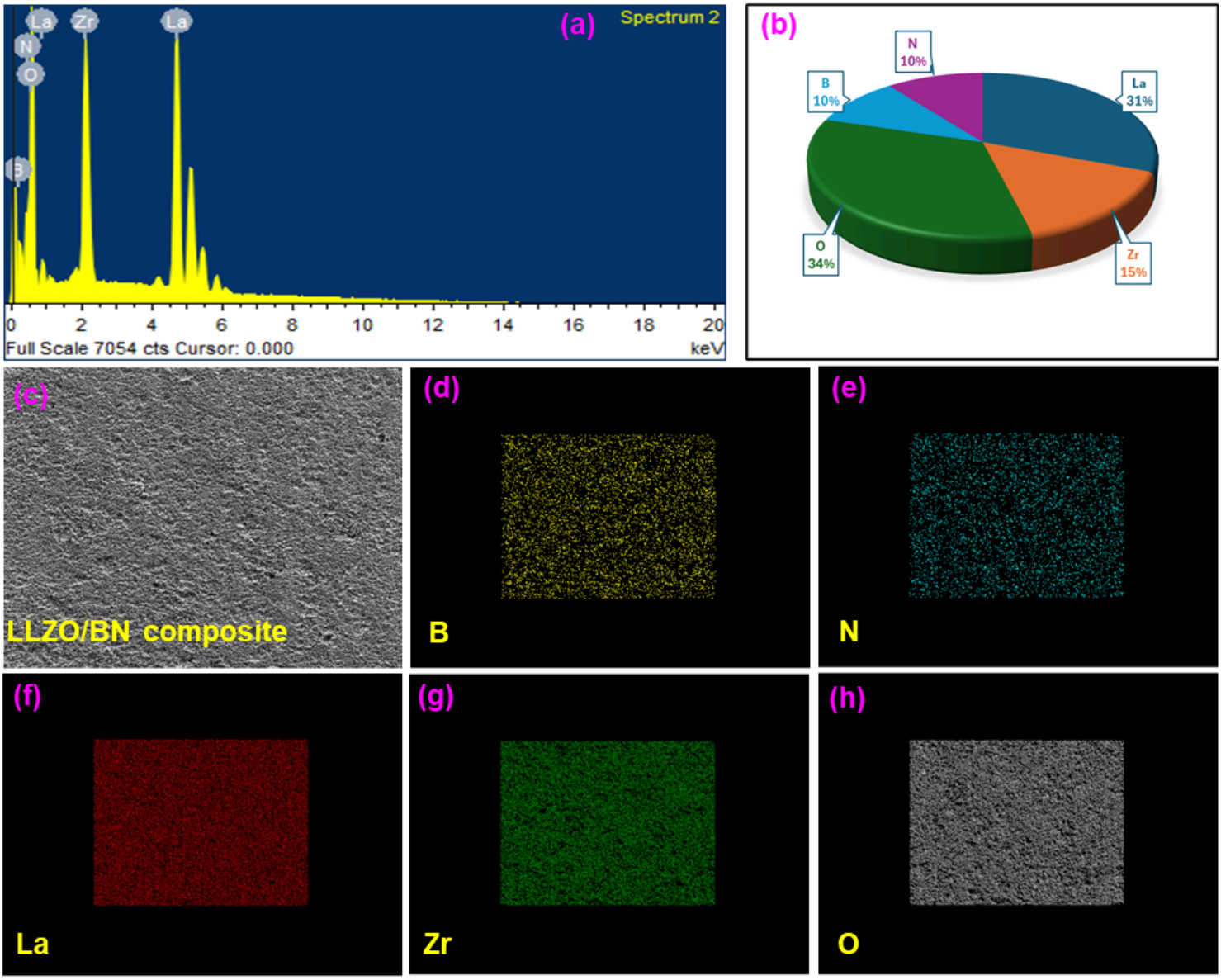

Figure 4

(a, b) EDX analysis and atomic weight percentage of all obtained elements in the LLZO/BN composite. (c) SEM image of the LLZO/BN composite. (d-h) Elemental mapping analysis of B, N, La, Zr, and O, respectively.

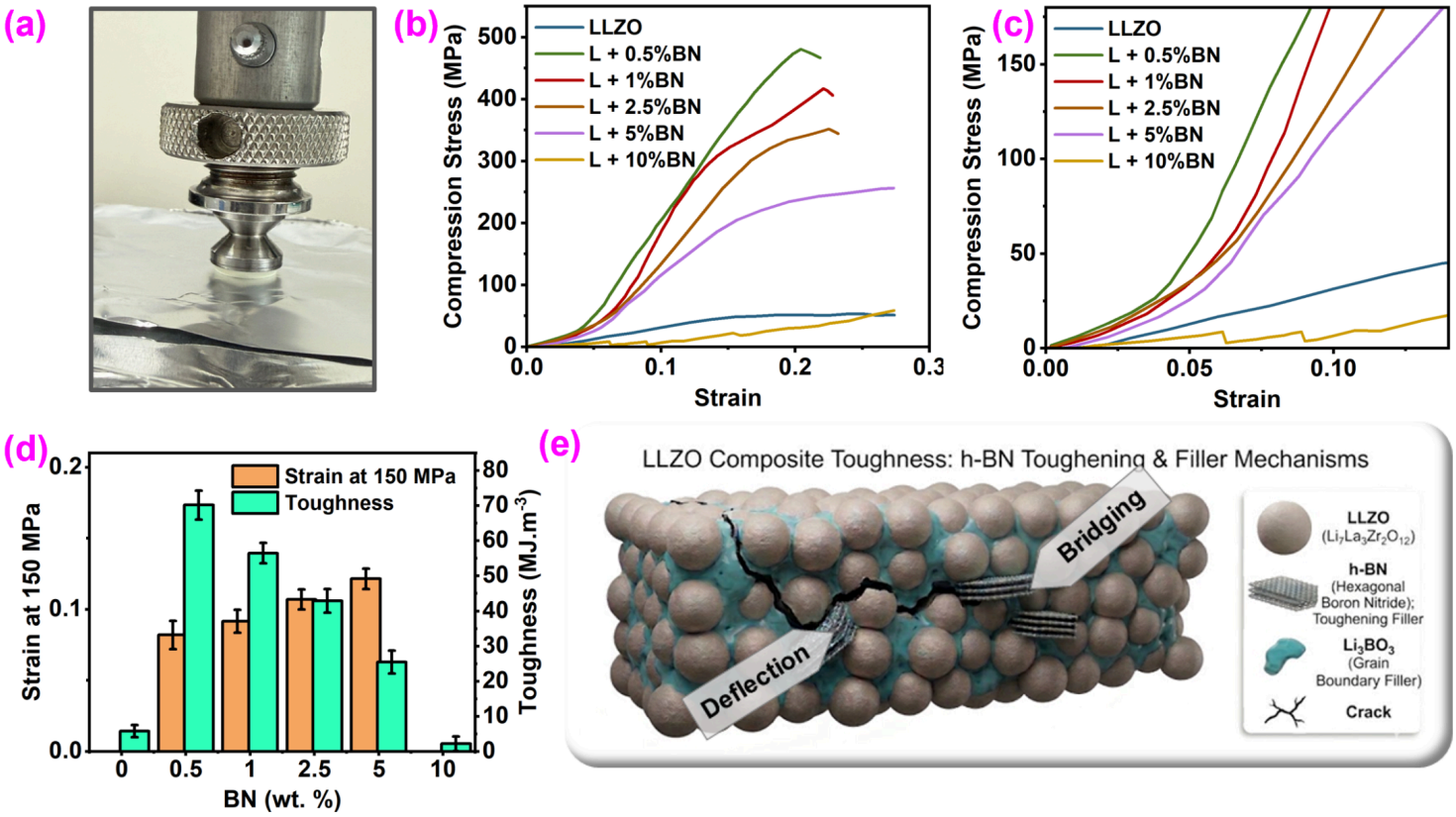

Figure 5

Mechanical properties of LLZO and LLZO/BN composites. (a) Experimental setup used for compression testing. (b) Compression stress-strain profiles of LLZO and LLZO/BN composites. (c) Magnified plot of stress-strain profiles. (d) Toughness and strain values at 150 MPa of LLZO and LLZO/BN composite pellets. (e) Schematic of crack bridging and deflection mechanism in LLZO/BN composite.

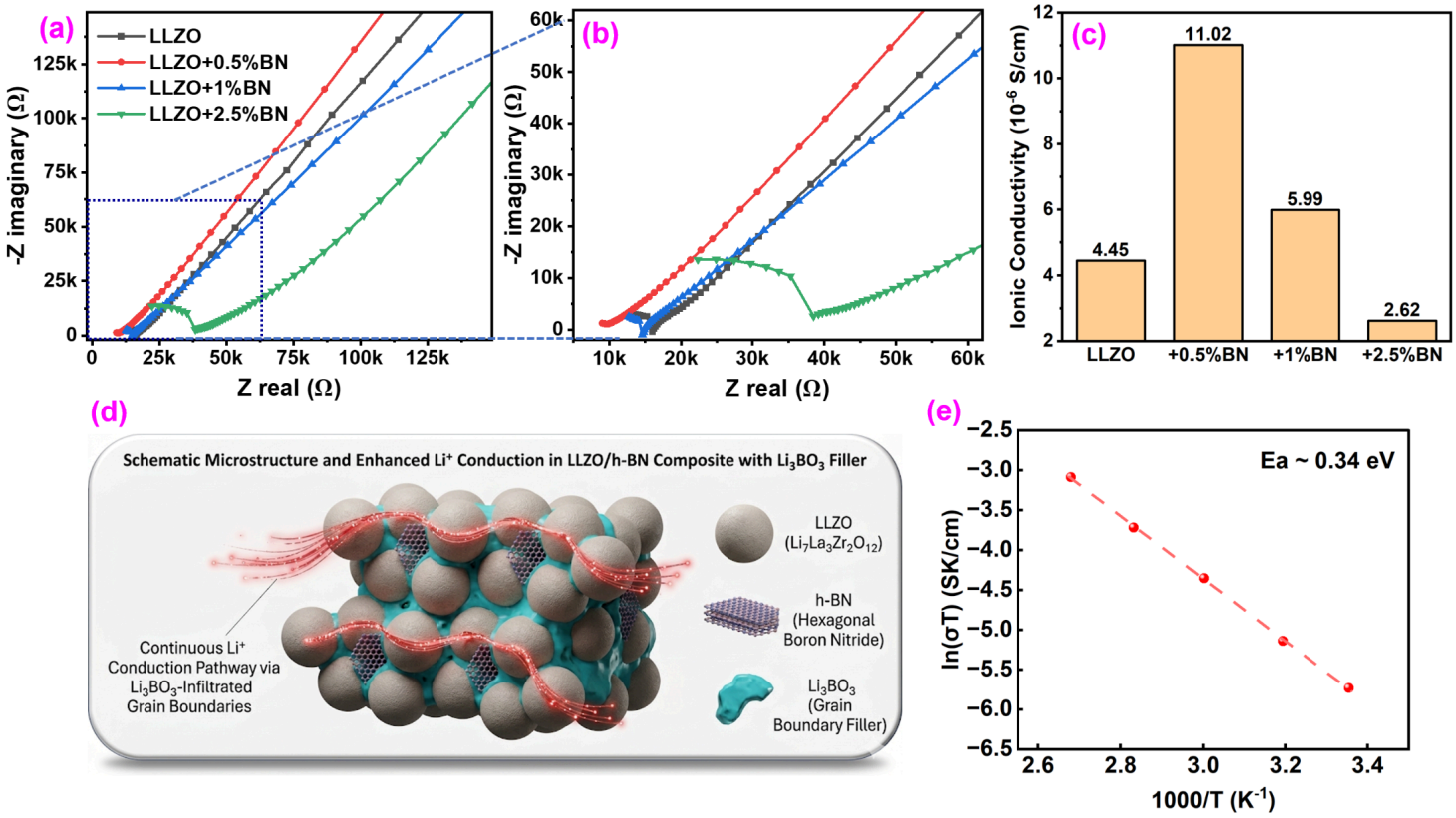

Figure 6

(a) Nyquist plots of pristine LLZO and LLZO/BN composites. (b) Zoomed-in view of Nyquist plots. (c) Ionic conductivity of LLZO and LLZO/BN composites. (d) Schematic illustration of improved Li-ion conduction in the LLZO/BN composite. (e) Arrhenius plot of LLZO/BN composite.

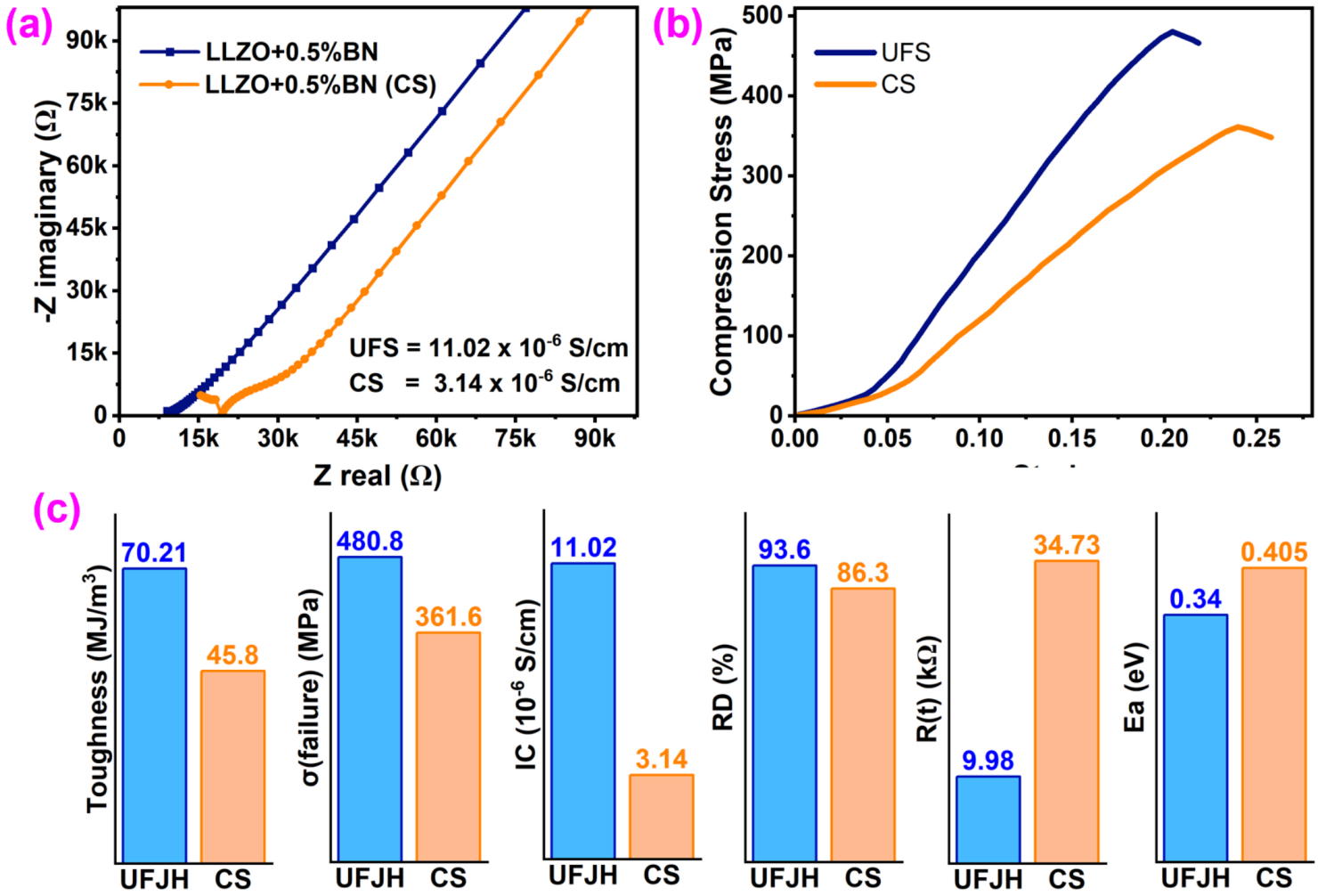

Figure 7

Comparison between UFJH and conventional sintering (CS) of LLZO + 0.5 wt.% BN pellets. (a) EIS Nyquist plots. (b) Compression stress. (c) Comparison of toughness, failure strength, ionic conductivity, relative density, total resistance, and activation energy of the samples prepared using UFJH and conventional sintering.

Supplementary Files

This is a list of supplementary files associated with this preprint. Click to download.

- SupplementaryData.docx